# Semiautomated Segmentation of Myocardial Contours for Fast Strain Analysis in Cine Displacement-Encoded MRI

Ting Chen*, *Member, IEEE*, James Babb, Peter Kellman, Leon Axel, and Daniel Kim

***Abstract*—The purposes of this study were to develop a semiautomated cardiac contour segmentation method for use with cine displacement-encoded MRI and evaluate its accuracy against manual segmentation. This segmentation model was designed with two distinct phases: preparation and evolution. During the model preparation phase, after manual image cropping and then image intensity standardization, the myocardium is separated from the background based on the difference in their intensity distributions, and the endo- and epi-cardial contours are initialized automatically as zeros of an underlying level set function. During the model evolution phase, the model deformation is driven by the minimization of an energy function consisting of five terms: model intensity, edge attraction, shape prior, contours interaction, and contour smoothness. The energy function is minimized iteratively by adaptively weighting the five terms in the energy function using an annealing algorithm. The validation experiments were performed on a pool of cine data sets of five volunteers. The difference between the semiautomated segmentation and manual segmentation was sufficiently small as to be considered clinically irrelevant. This relatively accurate semiautomated segmentation method can be used to significantly increase the throughput of strain analysis of cine displacement-encoded MR images for clinical applications.**

***Index Terms*—Energy minimization, magnetic resonance imaging (MRI), segmentation, strain.**

## I. Introduction

DISPLACEMENT-ENCODED magnetic resonance imaging (MRI) is a promising noninvasive modality for the quantification of intramyocardial function [1], [2]. Since its development in 1999, displacement-encoded MRI has undergone several improvements in the image acquisition, including: cine acquisition [3], echo-combined reconstruction [4], [5], through-plane motion encoding [6], parallel MR image acquisition and reconstruction [5], [7], and balance steady-state free precession (b-SSFP) readouts [5], [8], [9]. Despite these improvements in the image acquisition, the development of automated or semiautomated segmentation methods have been lagging [10], [11]. Currently, the manual segmentation of cardiac contours is the rate-limiting step in the strain analysis, since the subsequent steps, such as the phase unwrapping and finite element model analysis, do not require manual intervention. Therefore, the development of automated or semiautomated segmentation methods could increase the throughput of strain analysis of cine displacement-encoded MR images for clinical applications.

The automation of myocardial contour segmentation in short-axis images of the left ventricle (LV) is inherently difficult due to several anatomical and imaging factors. Anatomical factors that pose a significant challenge to accurately segment the cardiac contours include: 1) the proximity between the endocardial wall and papillary muscles, and 2) the ambiguous epicardial border caused by the liver and right ventricular (RV) insertion points. Additionally, cine displacement-encoded MR images of the heart have nonuniform image intensity, because they are typically acquired using surface receive coils (e.g., spatial variation of signal), and because their intensity decays as a function of cardiac phase due to the longitudinal relaxation of magnetization (e.g., temporal variation of signal).

Conventional semiautomated and automated segmentation methods can be classified into two generic categories: boundary-based and region-based. The boundary-based segmentation methods, such as the active contour [12]–[15] and level set methods [16], use the local image features (i.e., edges) to attract the evolving contours onto the target edges. However, these methods have several limitations. First, they usually require a manual initialization of the starting contour that must be relatively close to the true contour of the object, typically on an image-by-image basis, in order to avoid errors caused by local gradients. The manual initialization can be both inaccurate and tedious for large cardiac data analysis. Second, the epicardial and endocardial boundaries may act as each other's local minimum and cause the evolving contours to converge onto the wrong surface of the heart wall. Third, the resulting contours may be overly smooth due to the internal surface constraint. The region based segmentation methods [17]–[19] use the intensity distribution and/or texture distribution to separate the region-of-interest (ROI) from the background. In displacement-encoded MR images of the LV, the papillary muscles, the liver, and the chest wall have intensity distributions which are similar to that of the myocardium. As such, the region-based methods may "leak" into the background and produce inaccurate segmentation results for displacement-encoded MR images. Therefore, both the boundary-based and

Manuscript received September 15, 2007; revised December 10, 2007. First published February 8, 2008; last published July 25, 2008 (projected). *Asterisk indicates corresponding author.*

*T. Chen is with the Department of Radiology, New York University, 650 First Ave, New York, NY 10016 USA (e-mail: ting.chen@med.nyu.edu).

J. Babb, L. Axel, and D. Kim are with the Department of Radiology, New York University, New York, NY 10016, USA (e-mail: babbj01@endeavor.med.nyu.edu; leon.axel@nyumc.org; kimd10@endeavor.med.nyu.edu).

P. Kellman is with the Laboratory of Cardiac Energetics, National Heart Lung and Blood Institute, National Institutes of Health, Bethesda, MD 20892 USA (e-mail: kellmanp@nhlbi.nih.gov).

Digital Object Identifier 10.1109/TMI.2008.918327

region-based methods may be unsuitable for accurate segmentation of cardiac contours.

Hybrid segmentation frameworks [20]–[24] can overcome the limitations of the boundary-based and region-based methods by integrating the regional intensity and/or texture information and the boundary information into one generalized energy function for minimization. However, without the shape prior information, hybrid segmentation frameworks cannot exclude the papillary muscles from the LV. Shape priors [25]–[27] have been developed to guide the segmentation using the principal components analysis, but these methods are impractical for clinical applications because they typically require a large training set and a tedious training process. Therefore, conventional hybrid frameworks may be unsuitable for accurate segmentation of cardiac contours.

A recent hybrid framework that has been proposed to separate the papillary muscles from the endocardium is the STACS method [28]. This method uses a parametric shape prior together with the region and boundary information and integrates them into one generalized energy function for minimization, which is then driven by the calculus of variation under the framework of level set. The shape prior provides an external force to push the endocardial contour over local minima caused by papillary muscles. This method also includes an adaptive weighting process during the minimization of the energy function to improve its performance in the presence of image noise and artifacts. Compared with the manual segmentation results on mouse heart images, the STACS method has been shown to produce relatively accurate segmentation results. However, the STACS method may be suboptimal for cine displacement-encoded MR images of human heart due to several reasons. First, it requires a manual initialization of starting contours for every image, which is a limitation since a typical cine image set contains 18–22 frames. Second, its stochastic intensity model of the background is inaccurate. Third, its parametric shape prior cannot fully exclude papillary muscles. Fourth, the endocardial and epicardial surfaces are segmented separately in the STACS method, thereby increasing both the overall segmentation time and the likelihood of having the evolving contours converge onto the wrong surface of the heart wall. Therefore, there is a need to develop a customized segmentation method for cine displacement-encoded MRI.

The purposes of this study, therefore, were to develop a hybrid framework to semiautomatically segment the cardiac contours for cine displacement-encoded MRI and evaluate its accuracy against manual segmentation. The paper will be organized as follows. Section II will briefly describe the image acquisition and reconstruction of cine displacement-encoded MRI. Section III will describe the segmentation method. Section IV will describe the experiments and results. This paper will conclude with a discussion in Section V.

## II. Image Acquisition and Reconstruction

### A. Pulse Sequence

The improved cine displacement-encoded MRI pulse sequence [5] was implemented on a 3-T whole-body MR scanner (Tim Trio, Siemens Medical Solutions, Erlangen, Germany) equipped with a 12-channel phased array receive coil and a gradient system capable of achieving a maximum gradient strength of 45 mT/m and a slew rate of 200 T/m/s. Relevant imaging parameters include: spatial resolution $3.3 \times 3.3$ mm, slice thickness $7$ mm, temporal resolution $35$ ms, and breath-hold duration $12$ heartbeats. For additional details on the pulse sequence, see [5].

### B. Volunteer Imaging

Five healthy volunteers (two males; three females; min/median/max age $= 24/29/34$ years), with no history of heart disease and no risk factors for coronary artery disease, were imaged in three short-axis (apical, midventricular, basal) views of the heart. Human imaging was performed in accordance with protocols approved by the Human Investigation Committee at New York University, and all subjects gave written informed consent.

### C. Image Reconstruction

The image reconstruction was performed offline using Matlab (The Mathworks, Inc., Natick, MA). The root-sum-of-squares magnitude image was reconstructed and used for the segmentation algorithm. The displacement and the second principle strain $(E_2)$ maps were calculated from the phase images as previously described [3]–[5]. For details on the image reconstruction and strain calculation, see [3]–[5].

## III. Methods

We developed a hybrid framework integrating features of the STACS method [28] and new features to improve its segmentation performance for displacement-encoded MR images of the LV. Our segmentation model consists of two phases: 1) preparation and 2) evolution. During the model preparation phase, after manual image cropping and then image intensity standardization, the model is initialized automatically. During the model evolution phase, the model deformation is driven by the minimization of the energy function, which consists of five terms: 1) regional intensity distribution, 2) edges, 3) shape of the myocardium, 4) interaction between endo- and epi-cardial contours, and 5) smoothness of the evolving contours. An annealing algorithm [29] is implemented, as an extension of the previously described fitting algorithm [28], not only to adaptively weight the five terms in the energy function, but also to allow relaxation during the contour evolution to maximize the likelihood for a global solution to the energy function. Fig. 1 shows the overall flowchart of our segmentation method.

### A. Model Preparation

*1) Image Preprocessing:* Prior to image processing, one image per cine image set (typically end-systolic frame) was manually cropped (typical matrix size $\sim 30 \times 30$ pixels) with the centroid of the LV approximately coinciding with the centroid of the cropped image and the same image cropping was propagated to the remaining frames in the cine set. The manual image cropping was used to improve the overall time efficiency and separate the myocardium from irrelevant background features. To suppress random noise with minimal image blurring, we used a nonlinear multistage median filter with a $5 \times 5$ kernel [30]. To compensate for the temporally

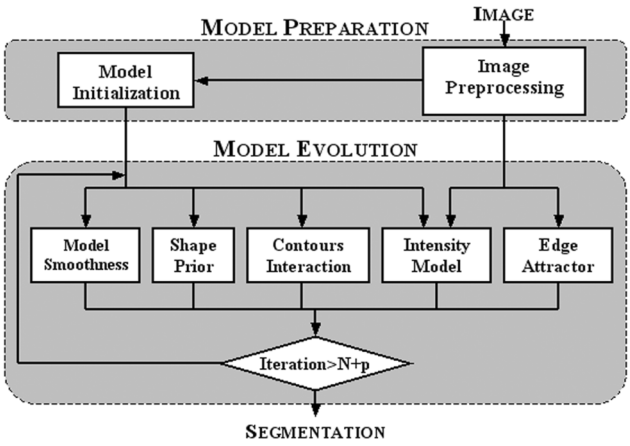


Fig. 1. Flow chart of our segmentation method. During the model preparation phase, after manual image cropping and then image intensity standardization, the myocardium is separated from the background based on the difference in their image intensity distributions, and the starting contours are initialized automatically using a Mumford-Shah functional based method. During the model evolution phase, the model deformation is driven by the minimization of the energy function consisting of five terms. An annealing algorithm is used to adaptively weight the five terms in the energy function to maximize the likelihood for a global solution to the energy function.

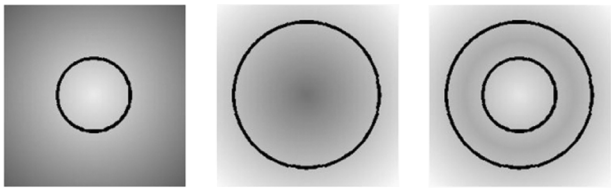


Fig. 2. Schematic diagrams of the initial boundaries: (a) $\phi_1$, (b) $\phi_2$, and (c) $\phi$.

nonuniform intensity, we calculated the mean intensity of the reference image (typically frame 2) in a cine image set and normalized the intensity of other images in the cine set by multiplying the factor $(I_{\text{ref}}/I_k)$, where $I_{\text{ref}}$ is the mean intensity of the reference image, and $I_k$ is the mean intensity of the $k$ th image in the cine set. To compensate for the spatially nonuniform intensity, we estimated the intensity profile across the image using a 2-D polynomial function and normalized the image intensity by dividing the images by the polynomial fitted intensity profile estimate, as previously described [31]. The combination of both spatial and temporal intensity normalizations converted the non-Gaussian myocardial intensity distribution to an approximate Gaussian distribution, whereas the background intensity distribution remained non-Gaussian.

*2) Level Set Model Definition and Initialization:* The endocardial surface, $C_1$, and the epicardial surface, $C_2$, can be embedded as the zero value in two level set functions $\phi_1(x,y)$ and $\phi_2(x,y)$, respectively

$$C_1 = \{(x,y) \in \Omega : \phi_1(x,y) = 0\} \quad (1)$$

$$C_2 = \{(x,y) \in \Omega : \phi_2(x,y) = 0\} \quad (2)$$

where $\Omega$ is the set of pixels in the image, $\phi_1$ is the 2-D distance map from the endocardial contour, and $\phi_2$ is the distance map from the epicardial contour. Fig. 2 shows a schematic diagram of the initial 2-D distribution for $\phi_1(x,y)$ and $\phi_2(x,y)$. We assign positive value to the interior, and the negative value to the exterior of $C_1$, and vice versa for $C_2$. The complete level set function is define as

$$\phi(x,y) = \max(\phi_1(x,y), \phi_2(x,y)). \quad (3)$$

The myocardium is

$$\Omega_1 = \{(x,y) \in \Omega : \phi(x,y) \leq 0\} \quad (4)$$

and the background is

$$\Omega_2 = \{(x,y) \in \Omega : \phi(x,y) > 0\}. \quad (5)$$

Given that $\phi$ is defined by the locations of $C_1$ and $C_2$, the level set function is initialized by finding the optimal location for $C_1$ and $C_2$ in target images using a Mumford-shah functional based method [32] (see Appendix for the mathematical details).

### B. Energy Function

During the model evolution phase, contours $C_1$ and $C_2$ deform under the influence of the image forces and the shape prior information. The evolution of the contours is equal to the evolution of the underlying $\phi$. We define an energy functional $J$ as a function of $\phi$, which is minimized when $C_1$ and $C_2$ converge onto their respective myocardial surface. Therefore, the segmentation problem is equal to the minimization of $J$, which is similar to (1) in [28] but with a new energy term

$$J(C) = \lambda_1 J_1(C) + \lambda_2 J_2(C) + \lambda_3 J_3(C) + \lambda_4 J_4(C) + \lambda_5 J_5(C) \quad (6)$$

where $J_1(C)$ incorporates the intensity distribution variation between the object and background, $J_2(C)$ is the edge attractor, $J_3(C)$ incorporates the new shape prior model of the heart wall that removes the papillary muscles, $J_4(C)$ controls the interaction between $C_1$ and $C_2$, $J_5(C)$ controls the smoothness of contours, and $\lambda_i$ is the weighting factor for the $i$th term. Compared with [28, eq. (1)], our energy function has a new term $J_4(C)$ and new definitions of $J_1(C)$ and $J_3(C)$. Since $C$ is defined as the zero level set of $\phi$, we can also rewrite the energy function in a similar formalism as [28, eq. (1)]

$$J(\phi) = \lambda_1 J_1(\phi) + \lambda_2 J_2(\phi) + \lambda_3 J_3(\phi) + \lambda_4 J_4(\phi) + \lambda_5 J_5(\phi) \quad (7)$$

*1) Intensity Stochastic Models:* After performing the intensity standardization, the myocardial intensity becomes approximately normally distributed, whereas the background intensity distribution remains non-Gaussian (Fig. 3). The myocardium is separated from the background based on the difference in their intensity distributions (see Appendix for the mathematical details).

A nonparametric model was used to describe the background intensity distribution because of the unknown number of background tissue types and their intensity distributions. Unlike a Bayesian based method (i.e., linear combination of

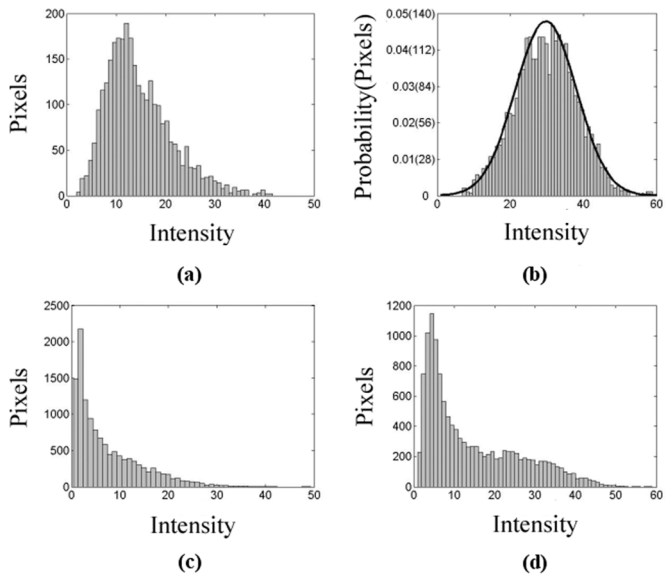


Fig. 3. Histograms of the myocardial and background intensities before and after intensity standardization: (a) myocardial intensity histogram before intensity standardization, (b) standardized myocardial intensity histogram after intensity standardization, (c) background intensity before intensity standardization, and d) background intensity after image standardization. Black line represents the corresponding Gaussian model of the myocardium intensity.

Gaussians [33]), which requires prior intensity information to effectively model the background, a nonparametric model is adaptive, straightforward, and relatively effective at defining non-Gaussian distributions.

*2) Edge Attractor:* The myocardial contours evolve and converge onto their respective wall surface during the energy functional minimization [28]. The corresponding energy term is described using [28, eq. (11)].

*3) Shape Prior:* In [28] and [34], the shape prior information is integrated into the segmentation algorithm by forcing the evolving contour $C_1$ to resemble an ellipse $C_H$. In the STACS method [28], all pixels are weighted equally during the endocardial contour estimation. We observed that concavities (e.g., pixels with negative curvature along $C_1$) are unlikely to be part of the endocardial contour. Hence, our shape prior includes another constraint to maintain surface convexity to effectively separate the papillary muscles from the heart wall. Specifically, pixels with negative curvatures on $C_1$ are eliminated from the estimation of the contour. This additional constraint prevents the contour from collapsing because of the increased contour convexity and maximization of area inside the closed contour. Compared to the previous shape priors [28], [34], this new shape prior has the advantage of effectively removing papillary muscles (see Fig. 4 for a comparison between shape priors).

To prevent overflow, level set evolution step sizes were controlled. For our self-adaptive shape model, we only use pixels on $C_1$ with positive curvatures $C_{1+}$, to estimate $C_H$.

$$C_{1+} = \left\{(x,y) : (x,y) \in C_1 \text{ and } \nabla \cdot \left(\frac{\nabla\phi_1(x,y)}{\|\phi_1(x,y)\|}\right) > 0\right\}. \quad (8)$$

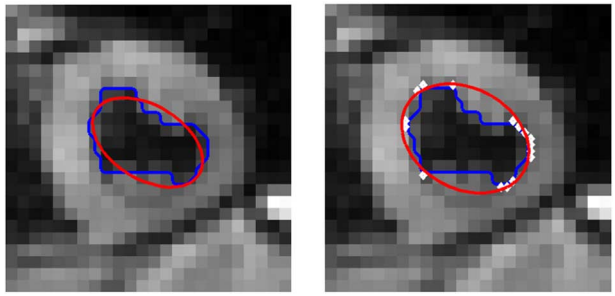

Fig. 4. Comparison between the (left) STACS method and (right) our segmentation method. The blue line represents the current evolving endocardial contour, and the red line represents the estimated shape model. The STACS shape model is estimated using all pixels on the current endocardial contour, whereas our method uses only pixels with positive curvatures (represented by white dots) on the current endocardial contour. The new method can effectively exclude the papillary muscles even though the current endocardial contour still includes the papillary muscles. Thus the new shape model provides a more accurate solution for the endocardial contour than the STACS shape model. The images are displayed with matrix size of 25 × 25 pixels.

To exclude erroneous pixels caused by local noise, we further eliminate singular pixels with positive curvature from $C_{1+}$ such that the final pixel set for the shape estimation is

$$C_1' = \{(x_k, y_k) : (x_k, y_k) \in C_{1+}$$

and

$$\exists (x_t, y_t) \in N(x_k, y_k)$$

such that

$$(x_t, y_t) \in C_{1+}\} \quad (9)$$

where $N(x,y)$ is the neighborhood of pixel $(x,y)$. We then integrate the shape information by forcing the minimization of the squared distance between the estimated contour $C_H$ and $C_1$. Fig. 4 illustrates the effectiveness of the new shaped prior to overcome the local minima caused by papillary muscles.

The convex hull or envelope of $C_1$ can also be used to find a subset of pixels on $C_1$ for the shape estimation. However, under the framework of level set segmentation, the positive curvature method may be superior to the convex envelope method. The curvature along $C_1$ is precalculated for the contour evolution in the level set framework such that no additional computation is needed to find the subset $C_1'$ using the curvature searching.

*4) Contours Interaction:* Unlike the original STACS method, in our method, the endo- and epicardial surfaces evolve simultaneously during the energy functional minimization, similar to the coupled propagation method.[35]. During the evolution process, these two contours emit external forces that prevent each other from being trapped at local minima. In the early stage of contour evolution, the contours interaction maintains a flexible distance between them by forcing the distance to approximate the average contour distance between them. In the last stage of the evolution, the weight of the contour interaction decreases to ensure that the contours can converge onto the edges of the heart wall with uneven thickness. As an additional constraint to prevent overflow or shrinkage of the myocardial area

in the final segmentation, the average distance between the contours must lie within a range that is proportional to the LV size.

Recall the definition of $C_2$ and $C_1$ as the epi- and endo-cardial surfaces, respectively, and $C = C_1 \cup C_2$. At any given time point, the average distance between the epi- and endo-cardial surfaces is calculated as

$$\begin{aligned} \text{average\_dist} &= \frac{\int_{C_1} \text{Dist}((x,y), C_2) ds}{\int_{C_1} ds} \\ &= \frac{\int_{C_2} \text{Dist}((x,y), C_1) ds}{\int_{C_2} ds} \end{aligned} \tag{10}$$

where $\text{Dist}((x,y), C_k)$ is the distance between a curve $C_k$ and a point $(x,y)$ (which is located on the other contour). We compute the distance map $\text{Dist}_k(x,y) = \text{Dist}((x,y), C_k)$ with respect to the endo- and epi-cardial surfaces. This enables us to define

$$D_k(x,y) = \text{Dist}_k(x,y) - \text{average\_dist}. \tag{11}$$

To account for a variable thickness of the heart wall, we use a quartic functional of $D_k$ in the energy term to allow small variations in thickness (i.e., for wall thickness within the range of average_dist $\pm$ 1) and give penalty to contours which are either too close or far from each other. A quartic functional performs better than a quadratic functional in our application because the penalty force enforced by the former and latter increase cubically (see Fig. 3) and linearly with $D_k(x,y)$, respectively. Compared with a quadratic functional, a quartic functional is relatively less sensitive to small variations and relatively more sensitive to large variations of heart wall thickness. Based on the definition of $D_k(x,y)$, we have the fourth term in the energy function

$$J_4(C) = \int_{C_1} D_2^4(x,y) ds + \int_{C_2} D_1^4(x,y) ds. \tag{12}$$

This term is equivalent to two sources that exert forces as illustrated in Fig. 5.

*5) Contour Smoothness:* We minimized the Euclidean arc length of the myocardial boundary $C$ to smooth the contour, as previously described by [28, eq. (27)].

*6) Overall Energy Functional:* By embedding $C_k$ as the zero level of $\phi$, the overall energy functional has the following form:

$$\begin{aligned} J(\phi, \phi_1, \phi_2) = \int_\Omega & \lambda_1 (M_1(1 - H_\varepsilon(\phi(x,y))) \\ & + M_2 H_\varepsilon(\phi(x,y))) \\ & + P_0(x,y)\delta_\varepsilon(\phi(x,y))|\nabla\phi(x,y)| \\ & + P_1(x,y)\delta_\varepsilon(\phi_1(x,y))|\nabla\phi_1(x,y)| \\ & + P_2(x,y)\delta_\varepsilon(\phi_2(x,y))|\nabla\phi_2(x,y)| dxdy \end{aligned} \tag{13}$$

$$\begin{aligned} M_k(x,y) &= -\ln(p_k(u(x,y))) \\ k &= 1, 2 \end{aligned} \tag{14}$$

where $H_z(\phi)$ is the Heaviside function, $\delta_\varepsilon(\phi) = (d/d\phi)H_\varepsilon(\phi)$ is the regularized delta function, $M_1$ and $M_2$ are the negative log of the myocardial and background intensities probability density function (pdf), respectively, and

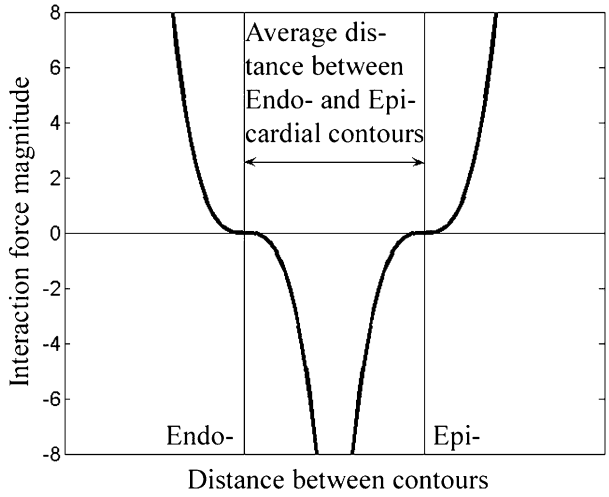


Fig. 5. Schematic diagram illustrating the interaction between the epi- and endo-cardial contours.

$$P_0 = \lambda_2 \gamma(x,y) + \lambda_5 \tag{15}$$

$$P_1 = \lambda_3 D^2(x,y) + \lambda_4 D_2^4(x,y) \tag{16}$$

$$P_2 = \lambda_4 D_1^4(x,y) \tag{17}$$

where the weighting factor $\lambda_k$ controls the relative strength of each term in the energy functional. With exception to the edge map $\gamma(x,y) = -|\nabla G(u(x,y))|$ (i.e., $G$ is the Gaussian operator), which is a static map derived from the image prior to the energy minimization, all other terms in the energy functional are dynamically updated during the evolution of the myocardial contours. $D$ is the distance between the current endocardial contour and the estimated ellipsoid; $D_1$ and $D_2$ are the distance maps from the endocardial and epicardial contours, respectively.

### C. Energy Function Minimization

*1) Recursive Minimization Framework:* Some terms in the energy functional (with variable $\phi$ or $C$) change during the model evolution. As such, the energy functional minimization is designed as an iterative process with two steps per iteration. The first step renews the energy function by estimating the new parameters for variable terms. The second step updates the myocardial contours in the form of the level set function $\phi$ (i.e., with $\phi_1$ and $\phi_2$ separated) based on the Euler-Lagrangian equation (see Appendix for the mathematic details).

*2) Annealing and Relaxation:* A simulated annealing algorithm was used to adaptively update the weighting factors during the energy minimization, in order to increase the likelihood that the energy function will achieve a global minimum (Fig. 6). The simulated annealing algorithm is divided into the following three phases: cooling, reheating, and relaxation.

*a) Cooling Phase:* $\lambda_1$ and $\lambda_2$ have relatively large values, $\lambda_3$ and $\lambda_4$ have relatively small values. During this phase, the segmentation is driven by the image information, while the shape prior and contour interaction act as weak constraints on the contours to avoid irregularity of the evolving contours.

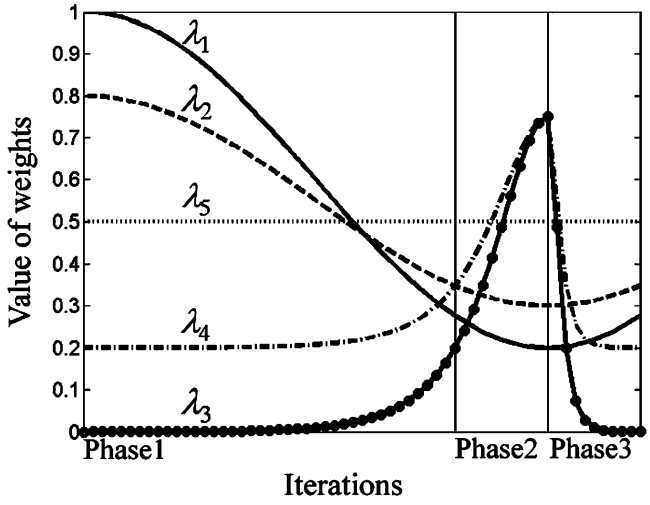


Fig. 6. The value of $\lambda_k$ during the simulated annealing. This annealing algorithm is used to adaptively weight the five terms of the energy function, in order to maximize the likelihood for a global solution to the energy function.

*b) Reheating Phase:* $\lambda_3$ and $\lambda_4$ increase dramatically as $\lambda_1$ and $\lambda_2$ decrease. Large $\lambda_3$ and $\lambda_4$ values enable the model to avoid local minima using the prior information on the heart shape and heart wall thickness. This phase pushes the model towards the global minimum of the energy function. Regional intensity and edges serve as weak constraints to ensure that the model will not move away from the object.

*c) Recooling or Relaxation Phase:* $\lambda_1$ and $\lambda_2$ increase again as $\lambda_3$ and $\lambda_4$ decrease rapidly towards their initial values. After the model has been pushed towards the global minimum, the shape prior is turned off to allow the contours to settle onto the local edges. We use the image information and the gradient descent method to converge the model onto its global minimum.

The weighting factors during the cooling and reheating phases are described as

$$\lambda_i(n) = \frac{1}{2}[\lambda_i(1) - \lambda_i(N)]\left[1 + \cos\left(\frac{n\pi}{N}\right)\right]$$

where

$$i = \{1, 2\}. \tag{18}$$

$$\lambda_i(n) = \frac{\lambda_i(N) - \lambda_i(1)}{\cosh\left[10 \cdot \left(\frac{n}{N} - 1\right)\right]} + \lambda_i(1)$$

where

$$i = \{3, 4\}. \tag{19}$$

$n$ is the current iteration number and $N$ is the total number of iterations in the cooling and reheating phases. We set $\lambda_1(1) = 1, \lambda_2(1) = 0.8, \lambda_3(1) = 0, \lambda_4(1) = 0.2, \lambda_1(N) = 0.2, \lambda_2(N) = 0.3, \lambda_3(N) = 0.75$, and $\lambda_4(N) = 0.75$ for $1 \leq n \leq N$.

We denote the number of iterations in the relaxation phase to be $p$. The formulation for $\lambda_1$ and $\lambda_2$ will not change for $N \leq n \leq N + p$. For $\lambda_3$ and $\lambda_4$, the formulation changes to

$$\lambda_i(n) = \frac{\lambda_i(N) - \lambda_i(N + p)}{\cosh\left[10 \cdot (n - Np)\right]} + \lambda_i(N + p)$$

where

$$i = \{3, 4\}. \tag{20}$$

$N + p$ is the total number of iterations. We set $\lambda_3(N + p) = 0$ and $\lambda_4(N + p) = 0.2$ for $N \leq n \leq N + p$. We note that $\lambda_5 = 0.5$ during the energy minimization.

To increase the confidence of the final energy minimization result, we empirically determined the values for $N$ and $p$ using several training data sets. A large $N$ can increase the likelihood that the energy functional achieves a global minimum, but at the expense of increased computation. Empirically, $N = 50$ was determined to be sufficient for segmenting myocardial contours, and $p = 10$ was determined to ensure that the energy functional will not move away from the global minimum. Fig. 6 shows the adaptive weighting of the energy function terms in the annealing algorithm.

## IV. Experiments and Results

### A. Qualitative Validation

We qualitatively compared the performance of our segmentation method against the manual segmentation and four other segmentation methods: 1) boundary-based segmentation driven by gradient vector fow (GVF) [15], 2) region-based segmentation by Chan and Vese [18], 3) hybrid Metamorpth framework [23], 4) and the STACS method [28]. Fig. 7 shows the segmentation results produced by these methods. This particular template image contains difficult segmentation features, including: papillary muscles and RV insertion points. Compared to the manual segmentation [Fig. 7(a)], different segmentation methods yielded markedly different results, even though they had all used identical initial contours. Specifically, the boundary-based segmentation driven by GVC failed to separate the papillary muscles from the myocardium and produced an overestimated endocardial contour due to its internal surface constraint, as well as distorted epicardial contour due to the local gradient caused by the endocardial surface [Fig. 7(b)]. Compared to the GVF method, Chan and Vese's algorithm produced more accurate segmentation in regions without difficult features. However, it failed to separate the papillary muscles from the endocardium and produced "leaked" results in the RV wall and liver [Fig. 7(c)]. The Metamorph method, using the scalar gradient [22] to improve its performance at concavities, produced more accurate results compared with the previous two methods [Fig. 7(d)]. However, it failed to separate the papillary muscles from the endocardium and produced slightly overestimated epicardium at the inferior RV insertion point. The STACS method produced more accurate results compared with the previous three methods [Fig. 7(e)]. However, it failed to separate one of the papillary muscles due to the limitation of its shape prior model and the lack of interaction between epi- and endo-cardial contours. Compared with the previous four segmentation methods, our segmentation method produced more accurate results with both the papillary muscles and RV insertions points separated from the myocardium. Fig. 8 compares the manual segmentation results and the

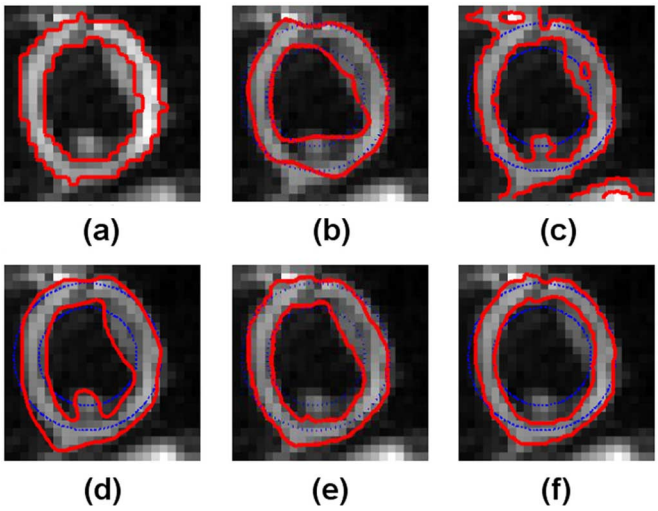


Fig. 7. Comparison between the different segmentation methods: (a) manual segmentation, (b) boundary based segmentation driven by GVF, (c) region intensity based segmentation using Chen and Vese, (d) hybrid Metamorph framework, (e) STACS framework, and (f) our segmentation framework. All segmentation methods (except manual) used identical initial contours derived from the zero level of the underlying level set function $\phi$ to perform a fair comparison. Red lines represent the segmentation results, and the dotted blue lines represent the starting contours. These images are displayed with matrix size of $24 \times 24$ pixels.

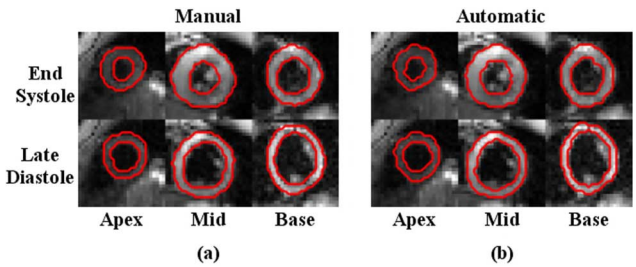


Fig. 8. Comparison between the (a) manual and (b) semiautomated segmentation outcomes at (top row) end systole and (bottom row) late diastole: (column 1) base, (column 2) midventricular, and (column 3) apex. Images are displayed with red lines, which represent the endo- and epi-cardial surfaces. These images are displayed with matrix size of $27 \times 27$ pixels.

corresponding results produced by our segmentation method in three short-axis views of the LV (apex, midventricular, base) at early systole, end systole, and late diastole. Fig. 9 shows representative displacement and $E_2$ maps generated using the manual segmentation and the corresponding results produced by our segmentation method. These two qualitative comparisons suggest that our segmentation method can reproduce the manual segmentation results.

### B. Quantitative Validation

We calculated the area similarity $S_{\text{area}}$ and shape similarity to evaluate the accuracy of our segmentation method against the manual segmentation on a pool of cine image sets of five volunteers (i.e., three short-axis views per subject; 294 total images). For simplicity, we chose one set of manual segmentation results by one reader as the "Gold Standard."

*1) Area Similarity:* We calculated the true positive (TP), true negative (TN), and false positive (FP) [36] and $S_{\text{area}}$[37] between the semiautomated segmentation and the manual segmentation. TP is the fractional amount of area that the semiautomated method correctly segmented relative to the area of the manual segmentation. TN is the fractional amount of area that the semiautomated method failed to segment relative to the area of the manual segmentation. FP is the fractional amount of area that the semiautomated method falsely segmented relative to the area of the manual segmentation. The FP-TN-TP system not only measures the overlapping area between two regions but also measures the relative contribution made by FP and TN. $S_{\text{area}}$ measures the overall segmentation performance and is defined as

$$S_{\text{area}} = \frac{2\text{TP}}{2 + \text{FP} - \text{TN}} \tag{21}$$

where $S_{\text{area}} > 0.7$ indicates an excellent agreement between two segmentations.

*2) Shape Similarity:* The shape similarity quantifies the difference in local orientation between two different segmentations, as previously described [28] and [38]. Compared with $S_{\text{area}}$, shape similarity is more sensitive to local variations in the object shape. For example, the inclusion of papillary muscles may cause a relatively small change in $S_{\text{area}}$ and a comparatively larger change in shape similarity. In cine displacement-encoded MRI, it is important to maintain the correct shape orientation because the underlying image contains region specific cardiac motion information. Therefore, we calculated the shape similarity as an additional measure to evaluate the performance of the segmentation method.

*3) Interobserver and Intraobserver Variability in Manual Segmentation:* We calculated the intraobserver and interobserver variability in manual segmentation using $S_{\text{area}}$ and shape similarity measurements, in order to evaluate the accuracy of the semiautomated segmentation method. For consistency, the papillary muscles were excluded from the manual segmentation.

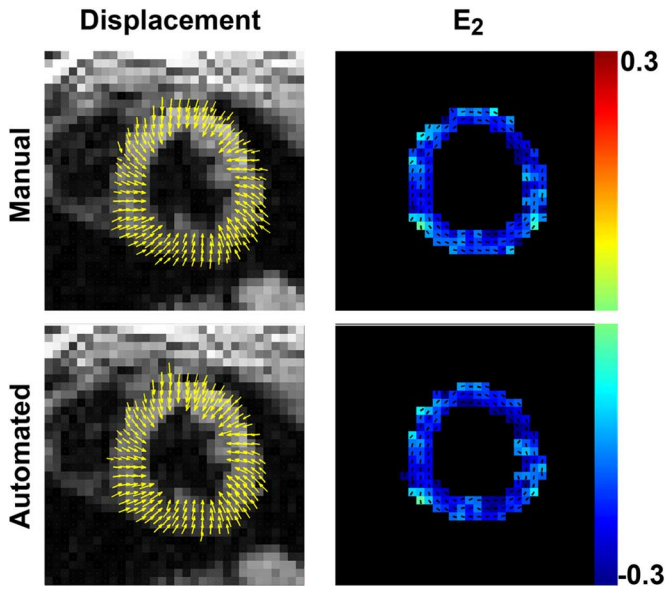


Fig. 9. Comparison of (left column) displacement and (right column) $E_2$ maps generated using the (top row) manual segmentation and the corresponding (bottom row) semiautomated segmentation. These images are displayed with matrix size of $32 \times 32$ pixels.

TABLE I
COMPARISON OF MEAN FN-TN-TP AND $S_{\text{area}}$ VALUES PRODUCED BY THE SEMIAUTOMATED AND MANUAL SEGMENTATION METHODS STRATIFIED BY LOCATION

| | Semi-Automated | | | | Manual | |
|---|---|---|---|---|---|---|
| Location | FN (%) | TN (%) | TP (%) | $S_{area}$ (%) | Inter-Var $S_{area}$ (%) | Intra-Var $S_{area}$ (%) |
| Apex | 14.7 | 10.3 | 89.7 | $88.0 \pm 3.6$ (Min: 79.4, Max: 94.9) | $89.3 \pm 3.3$ | $92.2 \pm 2.9$ |
| Mid | 7.1 | 13.2 | 86.8 | $89.6 \pm 2.3$ (Min: 82.9, Max: 94.2) | $90.3 \pm 2.3$ | $91.6 \pm 2.3$ |
| Base | 12.2 | 12.5 | 87.5 | $87.9 \pm 4.1$ (Min: 77.7 Max: 96.3) | $89.5 \pm 3.2$ | $92.4 \pm 2.6$ |
| All | 11.4 | 11.9 | 88.1 | $88.5 \pm 3.5$ (Min: 77.7 Max: 96.3) | $89.7 \pm 3.0$ | $92.0 \pm 2.6$ |

Comparison of mean FN-TN-TP and $S_{area}$ values produced by the semiautomated and manual segmentation methods stratified by location.

TABLE II
SUMMARY OF SHAPE SIMILARITY MEASURES FOR OUR SEGMENTATION METHOD AND THE INTRAOBSERVER AND INTEROBSERVER VARIABILITY IN MANUAL SEGMENTATION

| Location | $S_{shape}$ (%) | Inter- Variability (%) | Intra- Variability (%) |
|---|---|---|---|
| Apex | $85.0 \pm 6.2$ | $92.7 \pm 4.0$ | $94.9 \pm 3.1$ |
| Mid | $89.5 \pm 3.1$ | $92.8 \pm 3.2$ | $94.1 \pm 3.1$ |
| Base | $85.0 \pm 8.4$ | $93.1 \pm 3.4$ | $95.1 \pm 3.1$ |
| All | $86.5 \pm 6.6$ | $92.9 \pm 3.6$ | $94.7 \pm 3.1$ |

Summary of shape similarity measures for our segmentation method and the intra- and inter-observer variability in manual segmentation.

To calculate the intraobserver variability, one reader manually segmented the images and repeated the blinded segmentation two months later. To calculate the interobserver variability, the second reader performed the manual segmentation of the images. The two readers were blinded to each other.

Table I summarizes the FP-TN-TP and $S_{\text{area}}$ values calculated for our segmentation method and the intraobserver and interobserver variability in manual segmentation using $S_{\text{area}}$ measurements. The mean TP over subjects was 88.1%, which represents an excellent agreement in the object area and location, whereas the mean values of FN (11.4%) and TN (11.9%) were relatively small, indicating that the semiautomated segmentation results were neither overestimated nor underestimated. The mean $S_{\text{area}}$ over subjects was $88.5 \pm 3.5\%$, whereas the interobserver and intraobserver $S_{\text{area}}$ values were $89.7 \pm 3.0\%$ and $92.0 \pm 2.6\%$, respectively. Table II summarizes the shape similarity measures for our segmentation method and the intraobserver and interobserver variability in manual segmentation. The mean shape similarity over subjects was $86.5 \pm 6.6\%$, whereas the interobserver and intraobserver shape similarity values were $92.9 \pm 3.6\%$ and $94.7 \pm 3.1\%$, respectively.

For statistical evaluation, mixed model analysis of variance was used to assess and compare the segmentation methods (semiautomated segmentation versus interobserver variability in manual segmentation and semiautomated segmentation versus intraobserver variability in manual segmentation) with respect to the mean $S_{\text{area}}$ and the mean shape similarity measure within each location (apex, middle, and base) as well as the average over all locations. A separate analysis was conducted to compare the methods with respect to $S_{\text{area}}$ and in terms of the shape similarity measure. In each case, the data from all three methods were used as the dependent variable and the model included location and the indicator variable identifying measurements derived for the same ROI as classification factors. The variance–covariance structure was modeled by assuming observations to be correlated only when acquired from the same subject and by allowing the error variance to differ across methods and locations. Within this mixed model context, Tukey's honestly significant difference (HSD) procedure was used to compare each pair of methods while maintaining the overall type I error rate for the set of comparisons below the 5% level. Table III summarizes the $p$-values for each of the three locations and for the average over these locations. Although $S_{\text{area}}$ and the shape similarity measures of the semiautomated segmentation were observed to be in good agreement with those of the interobserver similarities, the results from the mixed model analysis indicate that the segmentation performance of our segmentation method is significantly different from that of the interobserver and intraobserver variability (HSD-adjusted $p - \text{values} < 0.0001$ for the mean over locations).

TABLE III
HSD-ADJUSTED TWO-SIDED $p$ VALUES FOR THE COMPARISON OF METHODS STRATIFIED BY LOCATION

| Measure | Location | Semi-Automated vs. Inter- Variability | Semi-Automated vs. Intra- Variability |
|---|---|---|---|
| Area | Apex | 0.0081 | <0.0001 |
| Area | Mid | 0.0184 | <0.0001 |
| Area | Base | 0.0004 | <0.0001 |
| Area | All | <0.0001 | <0.0001 |
| Shape | Apex | <0.0001 | <0.0001 |
| Shape | Mid | <0.0001 | <0.0001 |
| Shape | Base | <0.0001 | <0.0001 |
| Shape | All | <0.0001 | <0.0001 |

HSD-adjusted two-sided p values for the comparison of methods stratified by location.

Since even trivial differences can achieve statistical significance in the presence of superfluous statistical power, $S_{\text{area}}$ and the shape similarity measures were scrutinized to assess the magnitude of these differences and determine whether the significant differences can be considered clinically meaningful. Thus, 95% confidence intervals were generated for the difference between methods (semiautomated segmentation versus interobserver variability and semiautomated segmentation versus intraobserver observer variability) with respect to the mean of each measure ($S_{\text{area}}$ and shape similarity) in each location (apex, middle, and base) and averaged over all locations. The end points of a given interval provide an indication of how large or small the corresponding true difference may be and still be considered consistent with the observed data. As shown by the confidence intervals in Table IV, the data provide 95% confidence that the difference between semiautomated segmentation and the interobserver and intraobserver variability with

TABLE IV
LOWER AND UPPER BOUNDS OF THE 95% CONFIDENCE INTERVAL FOR THE DIFFERENCE BETWEEN METHODS (DENOTED BY INTER, INTRA, AND AUTO) STRATIFIED BY LOCATION. FOR EACH COMPARISON, THE UPPER BOUND CAN BE INTERPRETED AS THE LARGEST MAGNITUDE OF DIFFERENCE BETWEEN THE TRUE MEANS THAT IS CONSISTENT WITH THE DATA. THUS, IF THE UPPER BOUND CAN BE ACCURATELY DESCRIBED AS A CLINICALLY IRRELEVANT DIFFERENCE, THEN THERE IS 95% CONFIDENCE THAT THE TWO METHODS DO NOT DIFFER BY A CLINICALLY RELEVANT AMOUNT

| Measure | Location | Difference: Inter – Auto | | Difference: Intra – Auto | |
|---|---|---|---|---|---|
| | | Lower (%) | Upper (%) | Lower (%) | Upper (%) |
| Area | Apex | 0.5 | 2.3 | 3.5 | 4.9 |
| Area | Mid | 0.2 | 1.2 | 1.4 | 2.5 |
| Area | Base | 0.8 | 2.4 | 3.9 | 5.0 |
| Area | All | 0.5 | 1.5 | 2.9 | 3.9 |
| Shape | Apex | 6.3 | 9.1 | 8.6 | 11.2 |
| Shape | Mid | 2.4 | 4.2 | 3.6 | 5.5 |
| Shape | Base | 6.4 | 9.8 | 8.5 | 11.7 |
| Shape | All | 5.5 | 7.0 | 7.4 | 8.9 |

The lower and upper bounds of the 95% confidence interval for the difference between methods (denoted by Inter, Intra and Auto) stratified by location. For each comparison, the upper bound can be interpreted as the largest magnitude of difference between the true means that is consistent with the data. Thus, if the upper bound can be accurately described as a clinically irrelevant difference, then there is 95% confidence that the two methods do not differ by a clinically relevant amount.

respect to $S_{\text{area}}$ is no greater than 5% in any one location and is no more than 3.9% when averaged over locations. Thus, to the extent that a 5% difference might be considered clinically irrelevant, there is 95% confidence that the difference between the mean $S_{\text{area}}$ of our segmentation method and the means for each of interobserver and intraobserver variability is of little practical importance even though highly statistically significant. The data provide 95% confidence that the difference between the semiautomated segmentation and the interobserver and intraobserver variability with respect to the shape similarity is less than 10% when averaged over locations. Thus, to the extent that a 10% difference might be considered clinically irrelevant, there is 95% confidence that the difference between the mean shape similarity of our segmentation method and the means for each of the interobserver and intraobserver variability is of little practical importance even though highly statistically significant.

## V. DISCUSSION AND CONCLUSION

This study describes a hybrid framework that could be used for semiautomated segmentation of cardiac contours in cine displacement-encoded MRI. This framework combines features of the STACS method and new features to improve its overall segmentation performance. Our segmentation method consists of two phases: preparation and evolution. During the preparation phase, after manual image cropping and then after intensity standardization, the myocardium is separated from the background based on the difference in the intensity distribution, and a Mumford-Shah functional based method is used to automatically initialize the optimal starting boundaries of the endocardial and epicardial surfaces. During the model evolution phase, an energy functional minimization is used to drive the evolving contours to converge onto the corresponding myocardial surfaces. The validation analysis yielded a good agreement between the semiautomated and manual segmentation results (Tables I–IV). This relatively accurate semiautomated segmentation framework can be used to significantly increase the throughput of strain analysis of cine displacement-encoded MR images for clinical applications.

This method has several advantages. First, after minimal manual interaction of image cropping (one frame per cine image set), the coupled active contours are automatically initialized during segmentation (e.g., improves the overall time efficiency). Second, a nonparametric model of the background intensity distribution is used to separate the myocardium from the background. Third, a self-adaptive parametric shape prior model is used to avoid local minima (e.g., papillary muscles). Fourth, the epicardial and endocardial surfaces are simultaneously segmented with mutual interaction between them to prevent the contours from converging onto local minima. Fifth, a simulated annealing algorithm is incorporated into the energy function to adaptively weight the different terms in the energy function during minimization, in order to prevent the contours from being trapped at local minima. One limitation of this method is that image cropping is performed manually. However, image cropping can be automated by tracking the heart motion through the cardiac cycle, as previously described [28]. Another limitation of this study is that it did not include short-axis images of remodeled hearts with irregular shapes and long-axis images, which have different geometry than short-axis images.

Our segmentation method can be performed efficiently for typically cropped cine image sets (e.g., $27 \times 27 \times 22$ matrices). The computation time is less than 15 s for each cine set using a computer with 2-GHz CPU clock speed. The computational performance can be further improved using parallel programming.

The accuracy of our segmentation method depends on the overall image quality (e.g., spatial resolution, temporal resolution, signal-to-noise ratio), as well as the shape of the underlying heart. The test images were acquired using the improved cine displacement-encoded MRI at 3 T [5]. The performance of our segmentation method may be invalid for cases with poor image quality. On the other hand, further improvements in the image quality (e.g., pulse sequence development, shimming, and 32-channel cardiac array coils) may yield comparatively more accurate segmentation results by our segmentation method.

## APPENDIX

### A. Model Preparation

*1) Contour Initialization by a Mumford-Shah Method:* The contour initialization module is designed to minimize the energy function:

$$E(C|u_0) = w_1(A^+V^+ + A^-V^-) - w_2|\left(\mu \int_C |\nabla u_0|^2 dx\right) \tag{A1}$$

where weights $w_1 > 0, w_2 > 0$, and $w_1 + w_2 = 1, A^+$ and $A^-$ are areas of the object and the background, respectively, $V^+$ and $V^-$ are intensity variances in the object and the background, respectively, and $u_0$ is the observation of the image intensity. The variable $C$ in the energy function in (A1) is in the form of

two circles so that we can parameterize $C$ into $C(r_a, r_b, x, y)$, where $r_a > r_b > 0$ are the radii for circles corresponding to the epi- and endo-cardial surfaces and $(x, y)$ are the spatial coordinates of the centroid. To determine the optimal location for $C$, we minimize the energy functional in (A1) using the gradient descent method. The minimization process is computationally efficient, as well as intuitive, since the numerical solution for $(\partial E)/(\partial r_a), (\partial E)/(\partial r_b), (\partial E)/(\partial x)$, and $(\partial E)/(\partial y)$ are easy to compute when the shape of $C$ is fixed. The final $C$ is composed of two circles representing the endo- and epicardial surfaces so that we can use $C$ as the initial location for $C_1$ and $C_2$ and derive the level set function $\phi$ based on it.

### B. Energy Function

*1) Intensity Model:* The object intensity is modeled using the stochastic model described in [28]. The background consists of different tissues and, therefore, cannot be described by one normal pdf, as illustrated in Fig. 3. Hence, we use a nonparametric model to describe the background intensity. The two intensity distribution models are integrated into the energy function, as described in [28].

### C. Energy Function Minimization

*1) Recursive Minimization Framework:*

*Step 1: Parameter Estimation*. The terms that evolve along with the myocardial contours are $M_k, D_k$, and $D$. The derivation of $M_k$ is straight forward, so we will concentrate on the parameters $D_k$ and $D$. $D_1$ and $D_2$ : We first compute the average distance between endo- and epi-cardial contours using (10) and then use (11) to produce the interaction field for each myocardial contour. We compute the average distance in (10), because it can adapt with different data and self-adjust during the model evolution. Note that we preset an upper and a lower limit of the distance between the epi- and endo-cardial contours to be proportional to the LV size, in order to avoid contour collision and overflow.

Given the current $\phi$ and $C_1$, we calculate $\nabla \cdot ((\nabla\phi_1)/(\|\nabla\phi_1\|))$ along $C_1$, which resembles the curvature of $C_1$, and use it during the curve evolution. It has positive values at convexities and negative values at concavities. We select a convex subset of $C_1$ using (9) and estimate the shape of $C_H$. In the next step, we minimize the squared distance between $C_1$ and $C_H$ as previously described. [28]:

*Step 2: Contour Evolution*. Assuming all terms in the energy functional have been updated, we evolve the level set function $\phi$ (i.e., myocardial contours $C$) to minimize the energy functional. For convenience, the energy function (13) can be divided into two parts that correspond to the endocardial and epicardial contours, respectively. According to the calculus of variation [39], the Euler–Lagrange equation for the endo- and epi-cardial contours evolutions are

$$\left[\lambda_1(M_2 - M_1) - \nabla(P_0 + P_1) \cdot \left(\frac{\nabla\phi_1}{\|\nabla\phi_1\|}\right) - (P_0 + P_1)\nabla \cdot \left(\frac{\nabla\phi_1}{\|\nabla\phi_1\|}\right)\right] \delta_\varepsilon(\phi_1) = 0 \tag{A2}$$

$$\left[\lambda_1(M_2 - M_1) - \nabla(P_0 + P_2) \cdot \left(\frac{\nabla\phi_2}{\|\nabla\phi_2\|}\right) - (P_0 + P_2)\nabla \cdot \left(\frac{\nabla\phi_2}{\|\nabla\phi_2\|}\right)\right] \delta_\varepsilon(\phi_2) = 0 \tag{A3}$$

where

$$\nabla(P_0 + P_1) = \lambda_2\nabla\gamma + 2\lambda_3 D\nabla D + 4\lambda_4 D_2^3 \nabla D_2 \tag{A4}$$

and

$$\nabla(P_0 + P_2) = \lambda_2\nabla\gamma + 4\lambda_4 D_1^3 \nabla D_1 \tag{A5}$$

We solve $\phi_1$ and $\phi_2$ iteratively by replacing the right-hand side of (A2) and (A3) by $(d\phi_1)/(dt)$ and $(d\phi_2)/(dt)$. The partial differential equations governing the evolution of $\phi_1$ and $\phi_2$ are

$$\frac{d\phi_1}{dt} = \left[\lambda_1(M_1 - M_2) - \nabla(P_0 + P_1) \cdot \left(\frac{\nabla\phi_1}{\|\nabla\phi_1\|}\right) - (P_0 + P_1)\nabla \cdot \left(\frac{\nabla\phi_1}{\|\nabla\phi_1\|}\right)\right] \delta_\varepsilon(\phi_1) \tag{A6}$$

and

$$\frac{d\phi_2}{dt} = \left[\lambda_1(M_1 - M_2) - \nabla(P_0 + P_2) \cdot \left(\frac{\nabla\phi_2}{\|\nabla\phi_2\|}\right) - (P_0 + P_2)\nabla \cdot \left(\frac{\nabla\phi_2}{\|\nabla\phi_2\|}\right)\right] \delta_\varepsilon(\phi_2) \tag{A7}$$

where $\phi_1$ and $\phi_2$ are updated separately using the gradient descent method and then combined to update $\phi$ using (3). By separately calculating the curvatures of $\phi_1$ and $\phi_2$, we overcome the problem of sudden changes in function values caused by the maximum function. Furthermore, we restrict the calculation of the curvature within a narrow band centered at either $C_1$ or $C_2$, in order to speed up the computation and eliminate the impact of function discontinuities.

## ACKNOWLEDGMENT

The authors would like to thank D. Metaxas, Ph.D., of Rutgers University for helpful discussions on the segmentation model.

## REFERENCES

[1] A. H. Aletras, S. Ding, R. S. Balaban, and H. Wen, "DENSE: Displacement encoding with stimulated echoes in cardiac functional MRI," *J. Magn. Reson.*, vol. 137, pp. 247–252, 1999.

[2] A. H. Aletras and H. Wen, "Mixed echo train acquisition displacement encoding with stimulated echoes: An optimized DENSE method for in vivo functional imaging of the human heart," *Magn. Reson. Med.*, vol. 46, pp. 523–534, 2001.

[3] D. Kim, W. Gilson, C. Kramer, and F. Epstein, "Myocardial tissue tracking with two-dimensional cine displacement-encoded MR imaging: Development and initial evaluation," *Radiology*, vol. 230, pp. 862–871, 2004.

[4] D. Kim, F. H. Epstein, W. D. Gilson, and L. Axel, "Increasing the signal-to-noise ratio in DENSE MRI by combining displacement-encoded echoes stimulated echoes in cardiac functional MRI," *Magn. Reson. Med.*, vol. 52, pp. 188–192, 2004.

[5] D. Kim and P. Kellman, "Improved cine displacement-encoded MRI using balanced steady-state free precession and time-adaptive sensitivity encoding parallel imaging at 3 T," *NMR Biomed.*, vol. 20, pp. 591–601, 2007.

[6] F. H. Epstein and W. D. Gilson, "Displacement-encoded cardiac MRI using cosine and sine modulation to eliminate (CANSEL) artifact-generating echoes," *Magn. Reson. Med.*, vol. 52, no. 4, pp. 774–781, 2004.

[7] A. H. Aletras, W. P. Ingkanisorn, C. Mancini, and A. E. Arai, "DENSE with SENSE," *J. Magn. Reson.*, vol. 176, pp. 99–106, 2005.

[8] E. E. Bennett, V. M. Pai, and H. Wen, "Ultrafast DENSE technique for mapping the volumetric 3D wall motion of the left ventricle," in *Proc. 10th Annu. Meeting Int. Soc. Magn. Reson. Medicine*, Honolulu, HI, , 2002, p. 775.

[9] F. H. Epstein, S. Voros, W. D. Gilson, and C. M. Kramer, "Quantitative wall motion imaging by cine DENSE in acute myocardial infarction: Initial experience using an ssfp-based sequence," presented at the Proc. 7th Annu. Meeting Soc. Cardiovascular Magn. Reson., Barcelona, Spain, 2004.

[10] B. S. Spottiswoode, X. Zhong, A. T. Hess, C. M. Kramer, E. M. Meintjes, B. M. Mayosi, and F. H. Esptein, "Tracking myocardial motion from cine dense images using spatiotemporal phase unwrapping and temporal fitting," *IEEE Trans. Med. Imag.*, vol. 26, no. 1, pp. 15–29, Jan. 2007.

[11] B. Spottiswoode, X. Zhong, C. H. Lorenz, B. M. Mayosi, E. M. Meintjes, and F. H. Epstein, "Motion-guided segmentation of the left ventricle for cine DENSE MRI," in *Proc. 14th Annu. Meeting Int. Soc. Magn. Reson. Medicine*, Seattle, WA, , 2002, p. 794.

[12] L. D. Cohen, "On active contour models and baloons," *CVGIP: Image Understand.*, vol. 53, pp. 211–218, 1991.

[13] M. Kass, A. Witkin, and D. Terzopoulos, "Snakes: Active contour models," *Int. J. Comput. Vis.*, vol. 1, no. 4, pp. 321–331, 1988.

[14] D. Metaxas, *Physics-Based Deformable Models: Applications to Computer Vision, Graphics and Medical Imaging*. Norwell, MA: Kluwer Academic, 1996.

[15] C. Xu and J. L. Prince, "Snakes, shapes, and gradient vector flow," *IEEE Trans. Image Process.*, vol. 7, no. 3, pp. 359–369, Mar. 1998.

[16] R. Malladi, J. A. Sethian, and B. C. Vemuri, "Shape modeling with front propagation: A level set approach," *IEEE Trans. Pattern Anal. Mach. Intell.*, vol. 17, no. 2, pp. 158–175, Feb. 1995.

[17] D. H. Ballard and C. M. Brown, *Computer Vision*. New York: Springer, 1982.

[18] T. Chan and L. Vese, "Active contour without edges," *IEEE Trans. Image Process.*, vol. 10, no. 2, pp. 266–277, Feb. 2001.

[19] S. Z. Li, *Markov Random Field Modeling in Computer Vision*. New York: Springer, 1995.

[20] T. Chen and D. Metaxas, "Image segmentation based on the integration of markov random fields and deformable models," in *Proc. Med. Image Comput. Computer-Assisted Intervention (MICCAI)*, 2000, pp. 256–265.

[21] T. Chen and D. Metaxas, "A hybrid framework for 3D medical image segmentation," *Med. Image Anal.*, vol. 9, pp. 547–565, 2005.

[22] T. Chen, D. Metaxas, and L. Axel, "3D cardiac anatomy reconstruction using high resolution CT data," in *Proc. Med. Image Comput. Computer-Assisted Intervention (MICCAI)*, 2004, vol. 1, pp. 411–418.

[23] X. Huang, D. Metaxas, and T. Chen, "MetaMorphs: Deformable shape and texture models," in *Proc. IEEE Conf. Comput. Vision Pattern Recognit.*, 2004, vol. 1, pp. 496–503.

[24] S. Zhu and A. Yuille, "Region competition: Unifying snakes, region growing, and bayes/mdl for multiband image segmentation," *IEEE Trans. Pattern Anal. Mach. Intell.*, vol. 18, no. 9, pp. 884–900, Sep. 1996.

[25] T. Cootes, C. Taylor, D. Cooper, and J. Graham, "Active shape models-Their training and application," *Comput. Vision, Graphics, Image Process: Image Understanding (CVGIP)*, vol. 1, pp. 38–59, 1994.

[26] N. Paragios, "Shape-based segmentation and tracking in cardiac image analysis," *IEEE Trans. Med. Imag.*, vol. 22, no. 6, pp. 773–776, Jun. 2003.

[27] A. Tsai, A. Yezzy, W. Wells, C. Tempany, D. Tucker, A. Fan, W. E. Grimson, and A. Willsky, "A shape-based approach to the segmentation of medical imagery using level sets," *IEEE Trans. Med. Imag.*, vol. 22, no. 2, pp. 137–154, Feb. 2003.

[28] C. Pluempitiwiriyawej, J. M. F. Moura, Y.-J. L. Wu, and C. Ho, "STACS: New active contour scheme for cardiac MR image segmentation," *IEEE Trans. Med. Imag.*, vol. 24, no. 5, pp. 593–603, May 2005.

[29] G. Winkler, *Image Analysis, Random Fields and Dynamic Monte Carlo Metods*. New York: Springer-Verlag, 1995.

[30] A. Nieminen, P. Heinonen, and Y. Neuvo, "A new class of detail-preserving filters for image processing," *IEEE Trans. Pattern Anal. Mach. Intell.*, vol. PAMI-9-1, pp. 74–90, Jan. 1987.

[31] A. Madabhushi and J. K. Udupa, "Interplay of intensity standardization and inhomogeneity correction in MR image analysis," *IEEE Trans. Med. Imag.*, vol. 24, no. 5, pp. 561–576, May 2005.

[32] D. Mumford and J. Shah, Commun. Pure Appl. Math. "Optimal approximations by piecewise smooth functions and associated variational problems," 1989, vol. 42, pp. 577–685.

[33] A. A. Farag, A. S. El-Baz, and G. Gimel'farb, "Precise segmentation of multimodal images," *IEEE Transactions Image Process.*, vol. 15, no. 4, pp. 952–968, Apr. 2006.

[34] G. Aubert and P. Kornprobst, *Mathematical Problems in Image Processing. Partial Differential Equations and the Calculus of Variations*. Berlin, Germany: Springer-Verlag, 2001.

[35] X. Zeng, L. H. Staib, R. T. Schultz, and J. S. Duncan, "Volumetric layer segmentation using coupled surfaces propagation," in *Proc. 1998 IEEE Comput. Soc. Conf. Comput. Vis. Pattern Recognit.*, Santa Barbara, CA, Jun. 1998, pp. 708–715.

[36] J. Udupa, V. LeBlanc, H. Schmidt, C. Imielinska, P. K. Saha, G. J. Grevera, Y. Zhuge, L. M. Currie, P. Monholt, and Y. Jin, "A methology for evaluating image segmentation algorithms," in *Proc. SPIE: Med. Imag.*, 2002, vol. 4684, pp. 266–277.

[37] A. P. Zijdenbos, B. M. Dawant, R. A. Margolin, and A. C. Palmer, "Morphometric analysis of white matter lesions in MR images: Method and validation," *IEEE Trans. Med. Imag.*, vol. 13, no. 4, pp. 716–724, Dec. 1994.

[38] H. G. Barrow, J. M. Tenenbaum, R. C. Bolles, and H. C. Wolf, "Parametric correspondence and chamfer matching: Two techniques for image matching," in *Proc. 5th Annu. Int. Joint Conf. Artif. Intell.*, Aug. 1977, pp. 659–663.

[39] L. E. Elsgolc, *Calculus of Variations*. Reading, MA: Addison-Wesley, 1962.